

CANCER IMAGING

Simultaneous transrectal ultrasound and photoacoustic human prostate imaging

Sri-Rajasekhar Kothapalli^{1,2,3}, Geoffrey A. Sonn⁴, Jung Woo Choe⁵, Amin Nikoozadeh⁵, Anshuman Bhuyan⁵, Kwan Kyu Park⁵, Paul Cristman⁵, Richard Fan⁴, Azadeh Moini⁵, Byung Chul Lee⁵, Jonathan Wu⁴, Thomas E. Carver⁶, Dharati Trivedi⁴, Lillian Shiiba⁴, Idan Steinberg¹, David M. Huland¹, Morten F. Rasmussen⁵, Joseph C. Liao⁴, James D. Brooks⁴, Pierre T. Khuri-Yakub⁵, Sanjiv S. Gambhir^{1,7*}

Copyright © 2019
The Authors, some
rights reserved;
exclusive licensee
American Association
for the Advancement
of Science. No claim
to original U.S.
Government Works

Imaging technologies that simultaneously provide anatomical, functional, and molecular information are emerging as an attractive choice for disease screening and management. Since the 1980s, transrectal ultrasound (TRUS) has been routinely used to visualize prostatic anatomy and guide needle biopsy, despite limited specificity. Photoacoustic imaging (PAI) provides functional and molecular information at ultrasonic resolution based on optical absorption. Combining the strengths of TRUS and PAI approaches, we report the development and bench-to bedside translation of an integrated TRUS and photoacoustic (TRUSPA) device. TRUSPA uses a miniaturized capacitive micromachined ultrasonic transducer array for simultaneous imaging of anatomical and molecular optical contrasts [intrinsic: hemoglobin; extrinsic: intravenous indocyanine green (ICG)] of the human prostate. Hemoglobin absorption mapped vascularity of the prostate and surroundings, whereas ICG absorption enhanced the intraprostatic photoacoustic contrast. Future work using the TRUSPA device for biomarker-specific molecular imaging may enable a fundamentally new approach to prostate cancer diagnosis, prognostication, and therapeutic monitoring.

INTRODUCTION

Prostate cancer (PCa) is the most common nonskin cancer among men. More than 1.2 million cases are diagnosed worldwide each year, most often using the standard diagnostic approach in which an abnormal digital rectal exam or elevated prostate-specific antigen (PSA) in the blood prompts a transrectal ultrasound (TRUS)-guided prostate biopsy, where needles are placed blindly into the prostate because of an inability to reliably image PCa on US (1, 2). This approach leads to overdiagnosis of indolent tumors of little clinical relevance and underdiagnosis of some aggressive cancers (2). To address this clinical need, emerging in vitro diagnostic as well as in vivo imaging technologies have focused on detecting reliable biomarkers of PCa with high sensitivity and specificity (3–6), including three-dimensional (3D) TRUS-based imaging strategies for differentiating malignant prostate tissue using elastography (6) and angiography (7, 8). Among these, magnetic resonance imaging (MRI)-guided targeted TRUS biopsies tended to provide higher detection rate for clinically relevant PCa (9). Molecular imaging could further improve PCa care by allowing more accurate biopsies, and better assessment of tumor grade and aggressiveness, and help choose optimal management option (active surveillance, surgery, focal, or radiation therapy) for both clinically relevant and insignificant cases. Toward this goal, molecular imaging techniques such as hyperpolarized ¹³C MRI for mapping metabolic changes of PCa (10)

and positron emission tomography (PET) radiotracers for targeting PCa biomarkers (prostate-specific membrane antigen) (11) are being translated and evaluated in the clinic. However, MRI and PET are not suitable for frequent screening, monitoring, or real-time biopsy guidance due to their limited availability, high cost, and use of ionizing radiation in PET.

TRUS is nonionizing, inexpensive, portable, and widely available and is the current gold standard for guiding prostate biopsy. Although TRUS alone is not sufficient for reliable imaging of PCa, it is an ideal platform to integrate relevant molecular imaging strategies that could improve PCa visibility. Photoacoustic imaging (PAI) is a quintessential nonionizing method to pair with TRUS because they both share the same detection platform, and PAI provides complementary functional and molecular optical contrasts of deep tissue (up to 12 cm) with a submillimeter ultrasonic spatial resolution (12, 13). Hemoglobin absorption enabled high-contrast PAI of blood vasculature, associated angiogenesis, oxygen saturation, and total hemoglobin concentration (13–16); moreover, PA molecular imaging strategies that specifically target cancer biomarkers have been demonstrated to improve both diagnostic sensitivity and specificity in preclinical cancer models (17, 18). Over the past decade, PAI has evolved as a multiscale imaging technology, enabling in vivo imaging of structures ranging from organelles to organs (13), and has been translated to clinical studies by adapting existing clinical US devices for breast (19–21) and ovaries (22) to simultaneously enable PAI by attaching light guides to these devices. PAI studies on prostate had long been limited to animal imaging (23–25), such as imaging of implanted brachytherapy seeds inside the canine prostate (25); these were recently extended to clinical prostate imaging, wherein a single-wavelength (756 nm) PAI was performed for identifying a neurovascular bundle during invasive radical prostatectomy (26) and for imaging angiogenesis of prostate tumors during transrectal imaging of three patients with PCa (27, 28). Although these studies are encouraging, developing a transrectal device that compactly integrates

¹Molecular Imaging Program at Stanford and Bio-X Program, Department of Radiology, Stanford University School of Medicine, Palo Alto, CA 94305, USA. ²Department of Biomedical Engineering, The Pennsylvania State University, University Park, PA 16802, USA. ³Penn State Cancer Institute, Pennsylvania State University College of Medicine, Hershey, PA 17033, USA. ⁴Department of Urology, Stanford University School of Medicine, Palo Alto, CA 94305, USA. ⁵Department of Electrical Engineering, Stanford University, Palo Alto, CA 94305, USA. ⁶Edward L. Ginzton Laboratory, Center for Nanoscale Science and Engineering, Stanford University, Palo Alto, CA 94305, USA. ⁷Department of Bioengineering and Department of Materials Science & Engineering, Stanford University School of Medicine, Palo Alto, CA 94305, USA.

*Corresponding author. Email: sgambhir@stanford.edu

both US and optical components for in vivo deep-tissue molecular-specific multispectral PAI of the prostate is a key challenge.

Here, we report an integrated spectroscopic TRUS and PA (TRUSPA) device built using a relatively new class of miniaturized capacitive micromachined ultrasonic transducer (CMUT) arrays. We fully characterized the instrument and validated using tissue-mimicking phantoms, in vivo mouse models of PCa, ex vivo intact human prostates, and in vivo human prostate transrectal imaging ($n = 20$), including first-in-man contrast-enhanced prostate imaging using intravenous administration of the U.S. Food and Drug Administration (FDA)-approved indocyanine green (ICG) contrast agent ($n = 10$). Compared to the wide use of piezoelectric transducers in conventional US imaging, our CMUTs are designed and fabricated in-house using microelectromechanical systems (29, 30), and offer advantages such as wide bandwidth, improved signal-to-noise ratio (SNR) due to direct or proximal bonding with application-specific integrated circuits (ASICs), ease of fabricating large 1D (linear) as well as 2D arrays with 500 μm thickness (31–36), and high PA depth sensitivity (37).

RESULTS

We developed the TRUSPA device by tightly integrating a custom-made fused silica-silica fiber optic light guide and a custom-designed printed circuit board (PCB) that bonds a linear CMUT array to four ASICs (Fig. 1 and figs. S1 and S2). Design, description, and characterization of the CMUT array (64 elements, 5-MHz center frequency in immersion) are presented in table S1 and figs. S3 and S4. A gray-

colored polydimethylsiloxane (PDMS) lens coating on the CMUT array provides electrical insulation, mechanical stability, and elevational focusing (fig. S5) (38). As shown in fig. S1, a tunable nanosecond laser (Opotek Inc., 10-Hz pulse repetition rate, 5-ns pulse width, 680- to 950-nm wavelength range) was coupled to the fiber optic bundle of the TRUSPA device to deliver light deep into the prostate from different angles (39). A PC-based US imaging platform (Verasonics Inc.) was synchronized with the laser firing for an interleaved US and PA data acquisition and reconstruction using delay-and-sum beamforming (fig. S6). The TRUSPA system displays B-mode US (grayscale), PA (red color scale), and co-registered US and PA images in real time at 10 frames per second (fps) (movie S1).

Evaluation of the integrated TRUSPA system

Analysis on pulse-echo measurements from the PDMS-air interface for all 64 CMUT elements demonstrated that 6 elements lost wire-bonding contact during the PDMS encapsulation process, and that there was <1% variation in the PDMS thickness across all CMUT elements (fig. S5). We characterized the US field of the TRUSPA device using both Field II simulations (40) and a calibrated hydrophone (Onda HNP-0400) and measured ~ 2.5 MPa output focal pressure at the optimal bias voltage settings of 90-V DC and 30-V AC (figs. S7 and S8). Analysis of pulse-echo reflections from a flat metal target in immersion demonstrated that the TRUSPA device has a center frequency of 5 MHz and a 6-dB fractional bandwidth of about 80% (fig. S5D). The TRUSPA device provided optical fluence of ~ 10 mJ/cm² on the tissue surface, which is well within the American

National Standards Institute (ANSI) safety limit of 30 mJ/cm² at 800-nm wavelength (41). We evaluated the deep-tissue imaging capabilities of the TRUSPA device using a variety of biological tissue environments, including surgically removed human prostates. First, we demonstrated high geometric uniformity and co-registration accuracy of US as well as PA modes of the TRUSPA device by imaging a custom-made structural phantom (Fig. 2). The 10% intralipid, 1% agar, and 0.1% India ink-based phantom consisted of nine fishing wire targets (0.3 mm diameter) placed on and off axis at different depths and orientations inside the homogeneous background mimicking optical properties of prostate tissue with absorption and reduced scattering coefficients, respectively ($\mu_a = 0.1$ cm⁻¹ and $\mu_s' = 10$ cm⁻¹) (Fig. 2, A and B) (42). All wires generated US signal due to acoustic impedance mismatch with respect to the background, although some wires that were painted black absorbed photons and generated a PA signal (Fig. 2, C to E). We then imaged the phantom through a ~ 2.5 -cm-thick porcine tissue (boneless pork loin), to further increase scattering and heterogeneity, and demonstrated that all wire targets could still be imaged (Fig. 2, F to H). PA

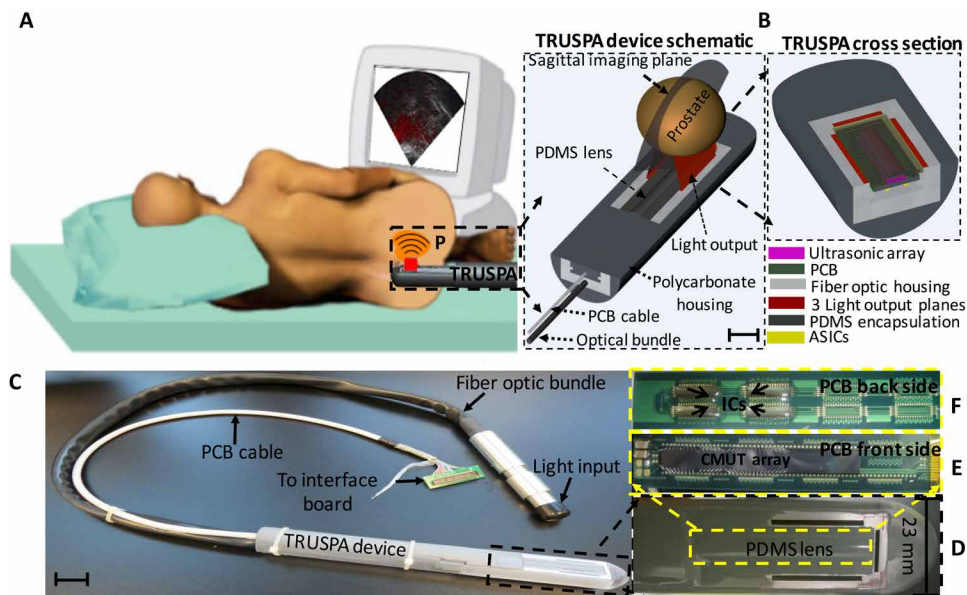


Fig. 1. Schematics and photographs of TRUSPA imaging of the human prostate. (A) Schematic representation of transrectal imaging of prostate (P) using the TRUSPA device. (B) Schematics of the distal end of the TRUSPA device and its cross section showing key components. PCB, printed circuit board; PDMS, polydimethylsiloxane; CMUT, capacitive micromachined ultrasonic transducer array; ASICs, application-specific integrated circuits. (C) Photograph of the TRUSPA device with a 23-mm scale bar. (D) Magnified photograph showing the distal end of the device that is inserted into the rectum of the patient. The three dark lines around three sides of the device are the output end of the optical fibers that deliver light into the prostate from three different planes [the red colored planes shown in (B)]. The device is encapsulated with a gray-color PDMS lens (yellow-dotted rectangular box) above the CMUT surface to achieve elevation focusing. (E and F) Images of the front (E) and back (F) sides of the custom-made PCB, underneath the PDMS lens, facilitating close bonding of the CMUT array with four ASICs. Figures S1 to S3 provide complete details of the TRUSPA imaging system.

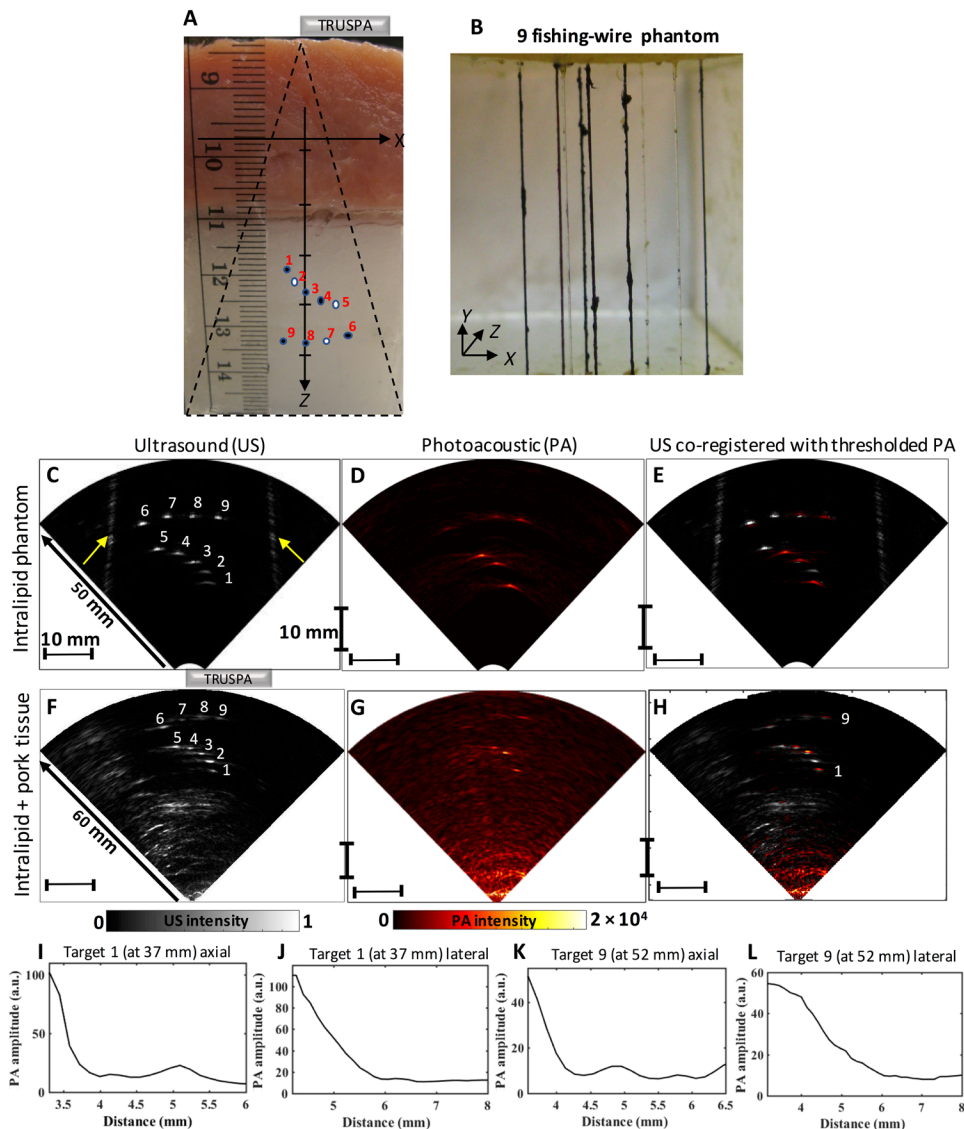


Fig. 2. Evaluating structural imaging capabilities and co-registration accuracy using a deep-tissue phantom. (A) Photograph showing the side view of a prostate tissue-mimicking intralipid phantom covered with a ~25-mm thick porcine tissue. The schematic positions of all nine fishing wire targets of 0.3 mm diameter, shown as dots, are as follows: 1 (12 mm, 20°), 2 (14 mm, 10°), 3 (16 mm, 0°), 4 (18 mm, -10°), 5 (20 mm, -20°), 6 (22 mm, -20°), 7 (22 mm, -10°), 8 (22 mm, 0°), and 9 (22 mm, 10°). The unit distance on the z axis is 10 mm. Blue dots represent wires painted black as shown in (B). (B) Photograph of an empty phantom tank before it is filled with intralipid solution. US, PA, and a co-registered US + PA images of the wire targets (C to E) inside the intralipid phantom and (F to H) when imaged through the porcine tissue. Yellow arrows point to US signals generated at the phantom edges. Plots of edge spread functions of target 1 (at 37 mm) along (I) axial and (J) lateral directions, and for target 9 (at 52 mm) along (K) axial and (L) lateral directions. a.u., arbitrary units. Scale bars, 10 mm (C to H).

data analysis on wire targets 1 and 9, at depths of 37 and 52 mm, respectively, from the surface of the porcine tissue, demonstrated SNRs of ~22 and 13 dB, axial resolutions of 0.32 and 0.34 mm, and lateral resolutions of 0.8 and 1.1 mm, respectively (Fig. 2, I to L).

Next, using fiducial tubes of blood or ICG placed in the mid (through the urethral opening) and anterior regions of excised human prostates, we demonstrated that the TRUSPA device can generate high-contrast and high-resolution PA images of hemoglobin and ICG molecules in the human prostate background, whereas US images displayed poor contrast of these fiducial tubes (Fig. 3). Table S2

summarizes the key TRUSPA imaging parameters quantified from US and PA signals in Figs. 2 and 3. In Fig. 3 (K to N), we present an example of ex vivo imaging of PCa on surgically removed human prostate obtained from a patient who underwent a radical prostatectomy as a routine standard of care. As shown in Fig. 3M, this patient had a fair amount of disease (1.1 cm, PIRADS 4) in the right lateral peripheral zone (PZ). This prostate was imaged using the TRUSPA device, and the malignant region was specifically targeted during the scanning. As shown in Fig. 3L, the co-registered PA/US image at 800 nm showed the boundary of the tumor mass (white circled region) in the right lateral PZ on the US image (grayscale) and strong PA contrast of ~20 dB, which was not present when scanned through other regions of the prostate. We imaged 20 surgically removed prostates to identify distinct PA features of PCa. Because there was a lot of blood loss from the prostatectomy, it was difficult to distinguish the malignant region in excised human prostates based on intrinsic PA contrast alone [unless the tumor(s) was preidentified on MRI and appeared hypoechoic on US at that location, as in Fig. 3L]. To further evaluate the TRUSPA system SNR as a function of imaging depth and laser wavelength, we imaged an Eppendorf tube of 8 mm diameter filled with ICG solution (1 mg/ml) at different depths (up to 5 cm) inside chicken breast tissue (fig. S9). These results demonstrated a linear decrease (~10 dB/cm) in the system SNR, ~34 dB at 18 mm to ~13 dB at 47 mm. The ICG spectral profiles from three different depths (18, 32, and 47 mm) demonstrated a decaying PA signal after 800 nm, similar to the standard ICG molar extinction spectrum. In future, a model-based fluence correction that accounts for depth and wavelength dependence will likely help in achieving higher spectral accuracies at deeper depths from the surface

(beyond 30 mm) needed for robustly quantifying the ICG distribution and perfusion. In addition, the PA contrast beneath the ICG tube in fig. S9 (I and L) was most likely due to blood absorption in the chicken tissue that shows similar PA intensity levels as the ICG tube, because of the higher optical fluence present at lower depths than at the depth of the ICG tube.

In the next step, we studied the in vivo detection of ICG by administering ICG solution (50 μ l at 2.5 mg/ml) intravenously into mice ($n = 5$) bearing subcutaneous PCa (PC3 cells) tumors and performed a simultaneous US and spectroscopic (multiwavelength) PAI

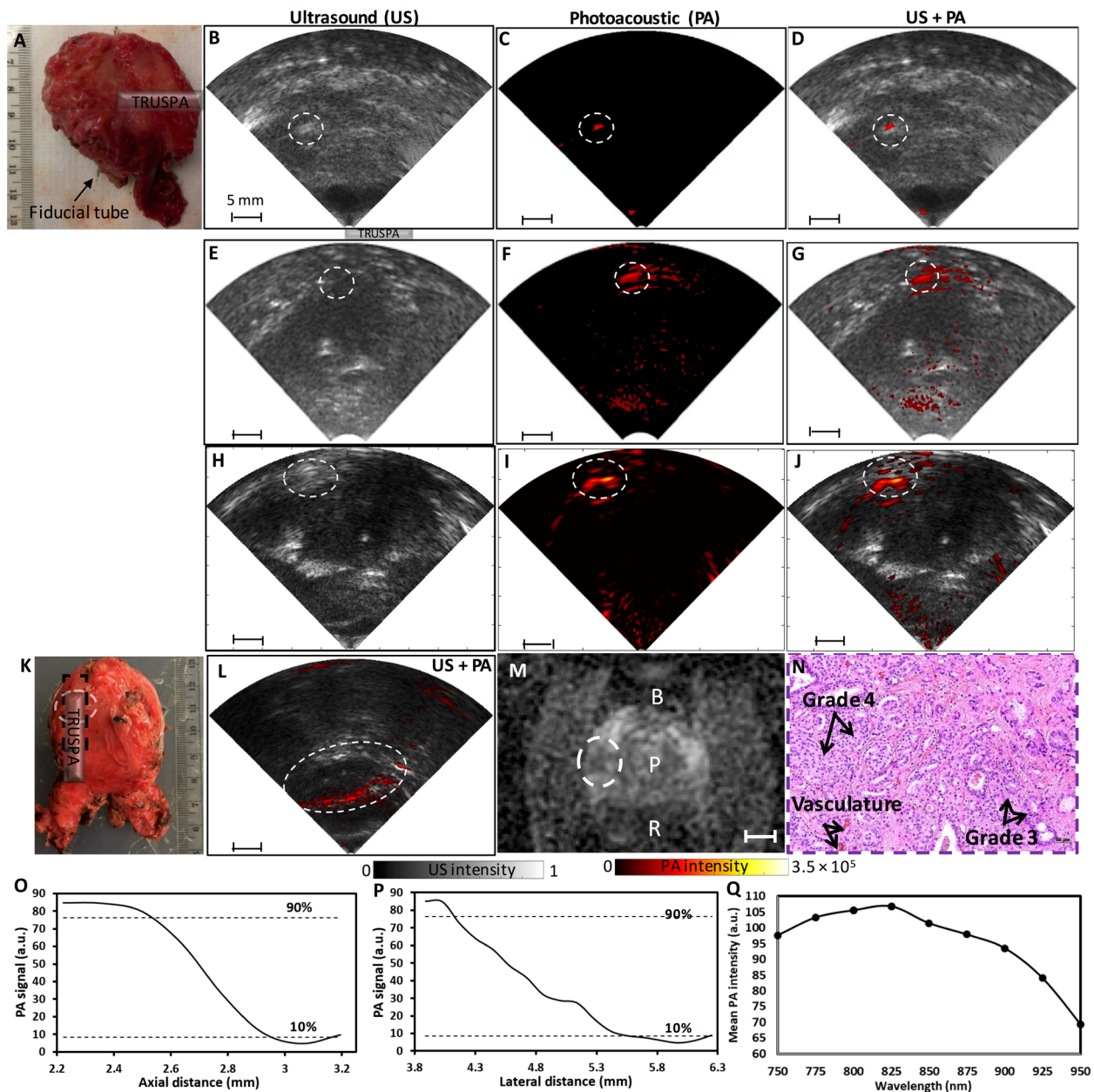


Fig. 3. TRUSPA studies on ex vivo intact human prostates after radical prostatectomy. (A) Photograph of a polyethylene fiducial tube (0.8 mm diameter) placed inside the urethra of an excised human prostate. Encircled regions in US (grayscale), PA (red color), and co-registered US + PA images show respective contrasts at 800-nm wavelength from (B to D) a blood-filled tube with a depth of ~2 cm inside the prostate, (E to G) a blood-filled tube placed behind the prostate covering an imaging depth of ~3.5 cm, and (H to J) a tube filled with ICG solution (1 mg/ml) placed behind the prostate. (K) Intact human prostate ex vivo showing the schematic orientation of the TRUSPA device when imaging the PIRADS 4 lesion (encircled region) in the right lateral PZ measuring 1.1 cm in diameter. (L) Co-registered US + PA image of the peripheral lesion (encircled). (M) Preoperative axial T2-weighted 3-T MRI showing low-intensity mass (encircled) in the right lateral PZ. B, bladder; P, prostate; R, rectum. Scale bar, 10 mm. (N) Histological tissue section from the peripheral lesion showing high cell proliferation (Gleason grades 3 and 4) and evidence of vasculature. Scale bar, 50 μ m. (O and P) Edge spread functions along the axial and lateral directions of the blood tube in (C) demonstrating resolutions (half the distance of X_{10-90}) of about 215 and 720 μ m, respectively. (Q) Spectral plot of the mean PA intensity of the ICG tube in (I) in the optical wavelength range of 750 to 950 nm, in steps of 25 nm. Scale bars, 10 mm (B to L).

using the TRUSPA device. US images showed the tumor boundary and other anatomical structures of the mouse, whereas the PA images (co-registered with the US) showed uptake of ICG dye in the tumor vasculature and inside the tumor region (Fig. 4). Spectral plots of pre- and post-ICG imaging, obtained from quantified mean PA contrast as a function of wavelength for five regions of interests

(ROIs; R1, R2, R3, R4, and R5 as defined in Fig. 4O) on multiwavelength pre- and post-ICG PA images (fig. S10), showed distinct trends, similar to a standard venous blood absorption and a mixture of blood and ICG spectra, respectively (Fig. 4, F to I). Furthermore, spectral unmixing on the multiwavelength PA data acquired during the pre- and the post-ICG injection periods (fig. S10) distinguished

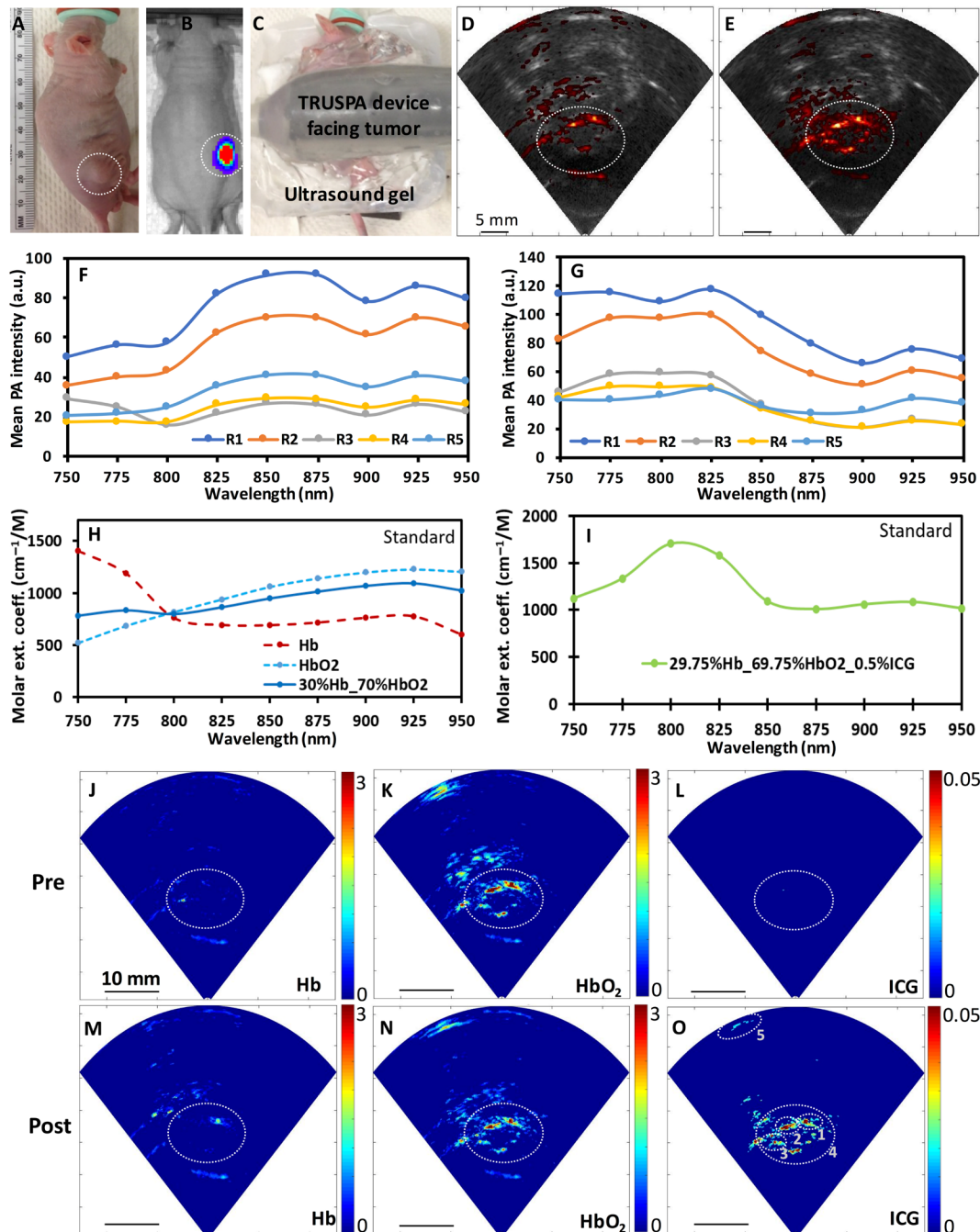


Fig. 4. In vivo imaging of a mouse prostate tumor using intravenous ICG. (A) Photograph of a mouse with a subcutaneous prostate tumor (PC3 cells expressing *Luciferase*). The tumor is encircled in white in all images. (B) Co-registered bioluminescence (color) and optical (grayscale) images of the mouse acquired using an IVIS 200 imaging system after intraperitoneal administration of β -*Luciferin*. (C) TRUSPA device was placed over the subcutaneous tumor using US gel during in vivo imaging. Co-registered US in grayscale and PA in color images of (D) pre-ICG and (E) 5-min post-ICG injection. Scale bars, 5 mm (D and E). Mean PA signal of five regions of interests [ROIs; defined in (O)] was calculated and plotted as a function of wavelength for (F) pre-ICG injection PA images shown in fig. S10A and (G) post-ICG injection PA images shown in fig. S10B. For comparison, the standard plots of molar extinction coefficient as a function of wavelength (taken from literature, <http://omlc.org/spectra/>) are plotted for (H) deoxyhemoglobin (Hb), oxyhemoglobin (HbO₂), and a mixture of 30% Hb and 70% HbO₂, and (I) a mixture of 29.75% Hb + 69.75% HbO₂ + 0.5% ICG. Spectrally unmixed images of Hb, HbO₂, and ICG (J to L) before ICG injection and (M to O) 5 min after ICG injection. Scale bars, 10 mm (J to O).

PA contrast originating from Hb, HbO₂, and the ICG molecules (Fig. 4, J to O). This difference in the trends between pre-ICG and post-ICG was used as one of the benchmarks to evaluate the presence of intravenously administered ICG during the TRUSPA imaging of

human prostate. Although the tumor region (encircled region) was found to be hypochoic on US, all PA contrast observed before ICG injection was likely due to absorption of hemoglobin present in the blood within vasculature of the tumor and surrounding regions. Comparison

of image contrast in the encircled tumor region in all unmixed images (Fig. 4, J to O) shows that ICG dye was taken up and retained inside the tumor region and surrounding vasculature, with a fourfold improvement in the PA contrast after ICG injection. The PA contrast and spectral profiles of pre- and post-ICG injection observed at deeper regions (ROI R5 at 35-mm depth shown in fig. S10, A and B) demonstrates the high optical sensitivity and spectral profiling capabilities of the TRUSPA device.

Pilot clinical TRUSPA imaging studies

With previous approval from the Stanford Institutional Review Board (IRB), we collected in vivo transrectal images of human prostates ($n = 20$) in US and PA modes of the TRUSPA device, including 10 subjects who received intravenous ICG during the TRUSPA imaging of the prostate. In vivo results demonstrated the capability of the device to simultaneously display anatomical information on the US, functional and molecular information on PA, and co-registered US + PA images of the prostate in real time at 10 fps (movie S1). The US images from the TRUSPA provided the sagittal anatomy of the prostate and surrounding tissue to a ~6-cm depth from the rectal wall with the $\pm 20^\circ$ field of view (FOV) (Fig. 5). From the PA images alone, the origin of optical contrast within the prostate remained unclear. However, the co-registered US + PA images, with overlaid anatomical and PA contrasts of prostate, demonstrated high PA contrast from dense vasculature adjacent to several prostatic structures. Neurovascular bundles in the posterior region (Fig. 5A), the dorsal venous complex that spans the prostate capsule, PZ, transi-

tional zone (TZ), the anterior zones (AZs) of the prostate (Fig. 5B), the seminal vesicles (Fig. 5B), and regions of suspicious hypoechoic mass (Fig. 5C) were identified. In Fig. 6, we present in vivo TRUSPA imaging results from a patient with proven PCa as evidenced on preoperative PET-MRI, using ^{68}Ga -labeled PET tracer targeting of bombesin on the PCa cells (43), and followed by PET-MRI contrast-targeted biopsy (with MRI-TRUS fusion) of the prostate using the conventional TRUS device. In agreement with the PET-MRI results, the TRUSPA device displayed a distinct PA contrast from the right peripheral base of the prostate, which was not present when scanned through other prostatic regions of this patient (movie S1).

The final imaging experiments involved contrast-enhanced TRUSPA imaging of human prostates using intravenous ICG (2.5 mg/ml) in the dose range of 5 to 75 mg ($n = 10$; table S3). In Fig. 7, we present in vivo TRUSPA prostate imaging results after intravenous ICG (25-mg dose) in a patient with biopsy-proven cancer in the left peripheral base of the prostate. To better evaluate the nature of ICG time activity, we applied principal components analysis (PCA) on the mean PA values of the 60-grid ROIs (fig. S11B) defined on each 800-nm PA image acquired during pre- and post-ICG injection period. The coefficient of the first PCA that accounts for 83% of the total variance in PA contrast as a function of time (relative to ICG injection) showed the time-activity curve with an average ICG arrival time of about 2.5 min and washout time of about 6 min after ICG injection, except from the left base of the prostate (Fig. 7G and fig. S11). These plots also show that the time activity is relatively higher in the left base of the prostate (having

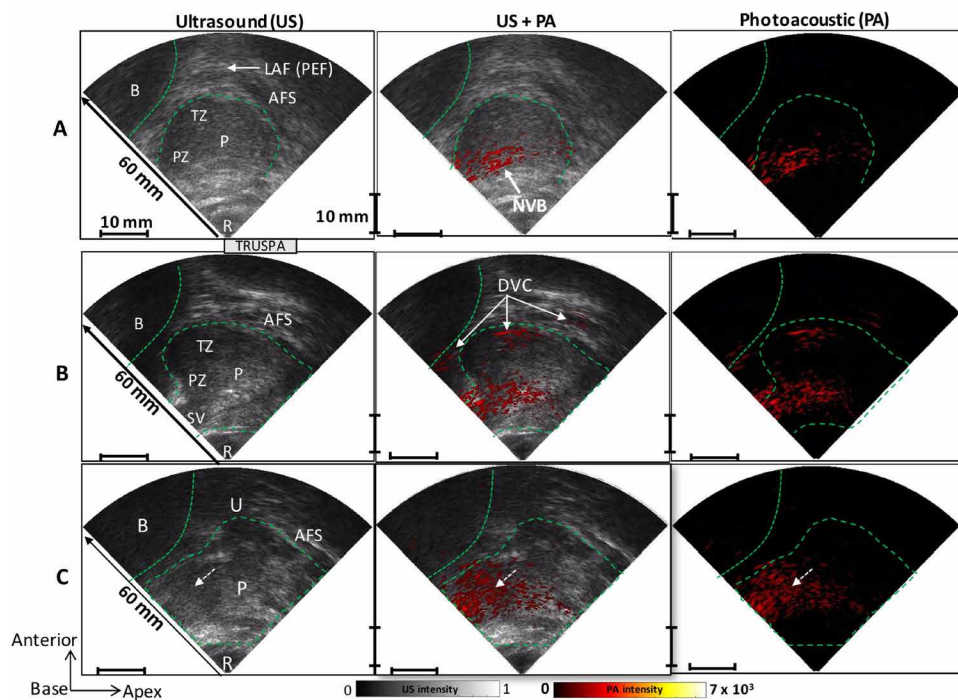


Fig. 5. In vivo TRUSPA imaging of human prostate. Each TRUSPA frame in (A) to (C) consists of US, PA, and co-registered US + PA images of human prostate. Scale bars, 10 mm. Prostate (P), rectum (R), bladder (B), urethra (U), peripheral zone (PZ), transition zone (TZ), seminal vesicle (SV), neurovascular bundle (NVB), anterior fibromuscular stroma (AFS), dorsal vascular complex (DVC), levator ani fascia (LAF), and parietal endopelvic fascia (PEF) were identified in these images. (A) PA contrast from the NVB (~20 mm depth) in the posterior PZ. (B) PA contrast from vasculature structures surrounding SV (~15 mm depth) and from DVC (~40 mm depth) that spans AFS, TZ, and PZ that is connected to the bladder neck. (C) PA contrast from a suspicious (white arrow) hypoechoic mass in the PZ in the left base of the prostate.

malignant region covered by ROIs 13 to 18 and 24 to 26) with 20% increase in the intraprostatic PA contrast after ICG injection. In addition, the spectral plots of mean PA contrast versus wavelength (Fig. 7H), using multiwavelength (750 to 950 nm, 25-nm step size) PA data acquired before and after intravenous ICG injection (fig. S12), showed different trends for pre- and post-ICG imaging, consistent with intravenous ICG results on mice models of PCa (Fig. 4). To further validate the presence of ICG within the prostate, we performed spectral unmixing of ICG from the Hb and HbO₂ using the multiwavelength PA data (fig. S12). The unmixed post-ICG image showed a distinct PA contrast with ~10% contrast enhancement from the left base of the prostate at peak ICG arrival time, with respect to the unmixed pre-ICG image (Fig. 7, I and J). A null hypothesis test on the contrast change between post- and pre-ICG unmixed images, defined as the ICG slope, of seven patients who underwent intravenous ICG (25 to 75 mg) resulted in statistically significant changes ($P = 0.009$) (Table 1). The ICG slope trend is like that of unmixed 800-nm image slope (the peak absorption wavelength of ICG) with $P = 0.578$, but not to that of unmixed 950-nm slope with

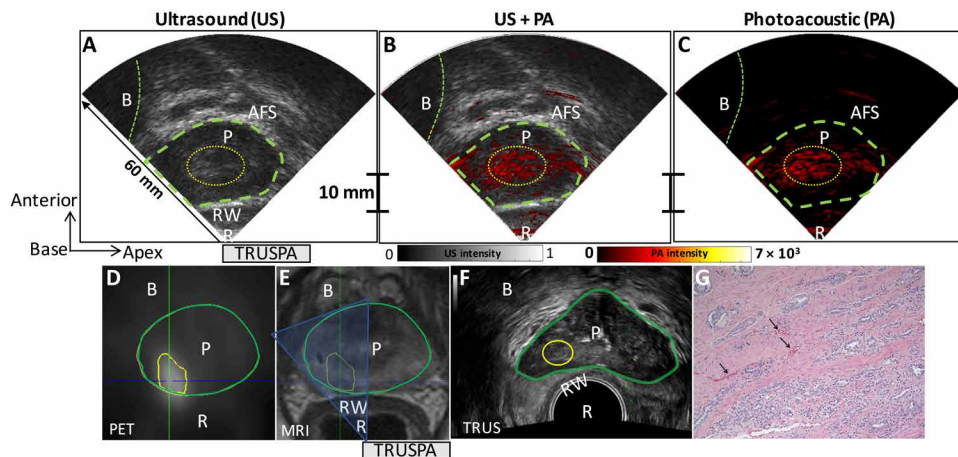


Fig. 6. In vivo multimodal PET, MRI, TRUS, and TRUSPA imaging of the prostate in a patient with PCa. In all images, the rectum (R), rectal wall (RW), bladder (B), anterior fibromuscular stroma (AFS), and prostate (P; green contour) are labeled. (A to C) Ultrasound (US) in grayscale, PA in red color scale, and co-registered US + PA images of human prostate obtained in vivo with the TRUSPA device. Movie S1 shows real-time TRUSPA imaging of this patient, which involved linear and rotational movements of the device in the rectum to scan different regions of the prostate. The suspicious region with distinct PA contrast [yellow contour in (A) to (C)] in the right base was repeatedly visited (around 25 to 35 s in the video) during the imaging session. (D) Axial PET imaging showing PCa (yellow contour) using ^{68}Ga -labeled radioactive tracer targeting bombesin receptor on the PCa cells. (E) Axial MRI showing anatomical information of the prostate with yellow contour covering the extent of PCa identified using PET molecular imaging. The TRUSPA FOV shown in (A) to (C) is also marked on the MRI (blue-shaded triangular region). (F) Axial TRUS image showing targeted region (yellow contour) for biopsy using the data from both MRI and PET; targeted biopsy confirmed PCa. (G) Final histopathology from the prostatectomy showing areas of hypervascularity (arrows) within the tumor. Scale bar, 10 mm.

$P = 0.110$ due to negligible absorption of ICG at 900-nm wavelength. Average percentage increases of 36 ± 22 for the 800-nm measurement and 9 ± 6.5 for unmixed ICG measurements were calculated ($n = 7$ patients). Furthermore, we observed a greater ICG contrast for patients with higher ICG doses of up to 75 mg (fig. S13). For the patient with the 5-mg dose, we observed negligible time activity of ICG and contrast improvement in the unmixed ICG image (fig. S14).

DISCUSSION

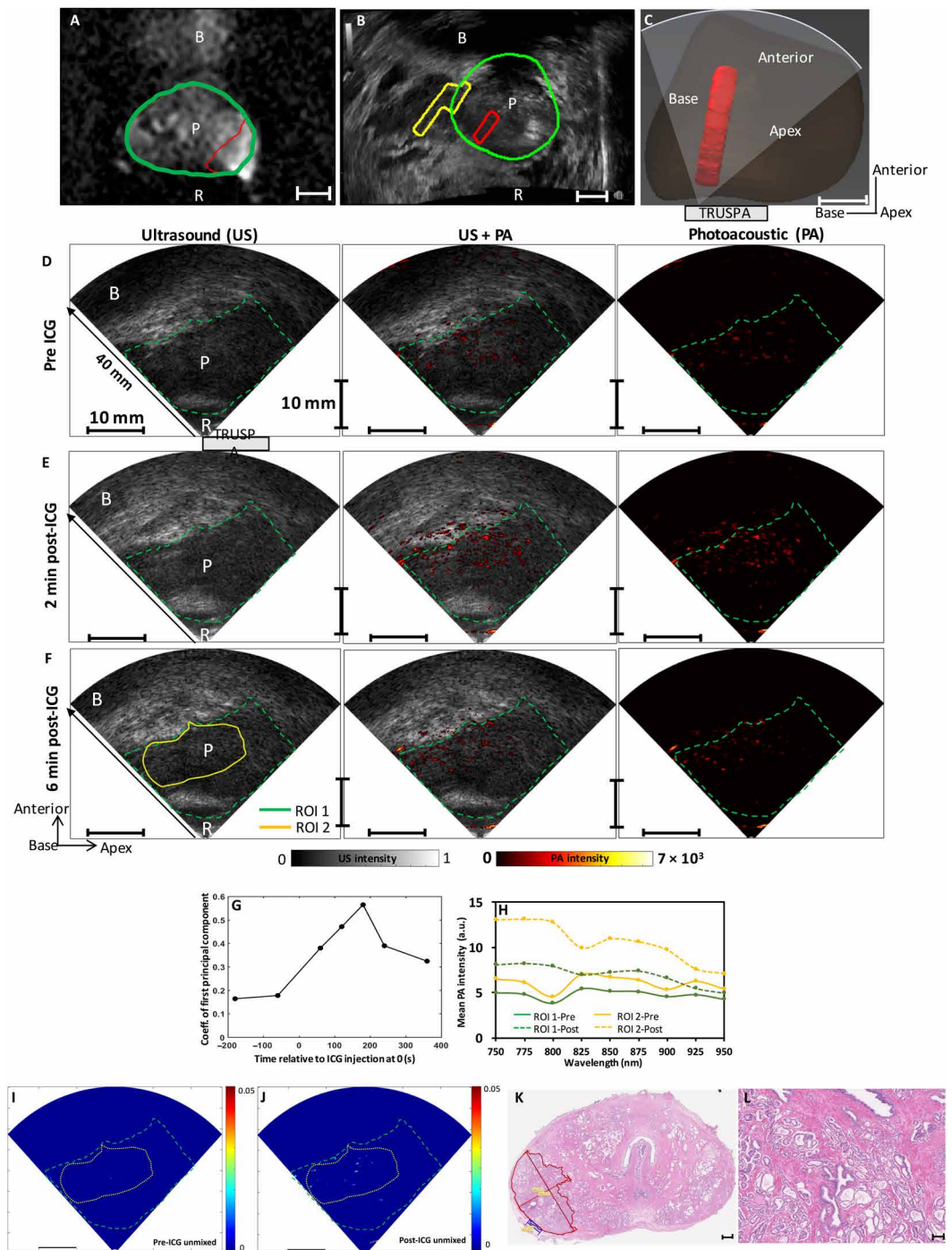
We report the development and the initial clinical use of an integrated TRUSPA device capable of simultaneously imaging US-based prostatic anatomy and PA-based functional and molecular optical contrasts in human subjects. Compact bonding of the CMUT array to the ASICs not only improved the noise floor but also provided enough room around the array to optimally distribute fiber optic cables for delivering light deep into the prostate from different angles. High receive sensitivity and near 100% fractional bandwidth of the CMUTs (31–36) further contributed to the high PA sensitivity observed in our TRUSPA experiments. A compact TRUSPA architecture that tightly integrates both optical and ultrasonic components is required given the space constraints for transrectal imaging of the prostate. Deep prostate PAI is not easily achieved by attaching a fiber optic light guide to the existing clinical TRUS devices that use lead zirconate titanate (PZT) arrays. Our approach overcame challenges such as lower depth and molecular sensitivity of previous PAI studies (26–28) and demonstrated multispectral imaging of intrinsic and extrinsic molecular PA contrast in the range of 3 to 4 cm inside the human prostate. Wider FOV and finer structural details seen on clinical TRUS devices (due to large aperture size, higher number of elements, and higher center

frequency of curvilinear PZT array) can be extended to future TRUSPA designs by using a linear/curvilinear CMUT array of comparable parameters (31–33). Furthermore, highly sensitive and large 2D (matrix) CMUT arrays could be implemented for real-time 3D imaging of prostate, covering both sagittal and axial views at the same time.

In pilot clinical studies involving several patients, the real-time co-registration of US and PA images allowed simultaneous mapping of local optical absorption of hemoglobin contrast in PA images to several prostatic structures identified on US images, such as seminal vesicles, neurovascular bundles, dorsal venous complex, and prostate capsule. Although contrast-enhanced ultrasonic techniques such as Doppler US are capable of indirectly mapping blood vessels, these techniques based on blood flow velocity have poor spatial resolution and lower sensitivity compared to PAI, which has demonstrated high sensitivity to detect single blood cells (44). For one patient with advanced PCa, TRUSPA demonstrated a distinct intrinsic PA contrast from the malignant region of the prostate,

confirmed by simultaneous PET-MRI and subsequent targeted biopsy results. We also studied ICG contrast-enhanced prostate imaging as the best possible first clinical step toward understanding the extrinsic molecular PA sensitivity of TRUSPA in humans. Using plots of time activity (PA contrast at 800 nm versus time), multispectral analysis (PA contrast versus wavelength), and spectrally unmixed ICG imaging, we observed dose-dependent (up to 75 mg total at 2.5 mg/ml) PA contrast enhancement of prostate. Comparison of spectrally unmixed images of Hb, HbO₂, and ICG in clinical and preclinical studies showed that the origin of the PA contrast in ICG images can be attributed to vascular space, because ICG rapidly binds to plasma proteins in the vasculature (45–47). Although the ICG activity and contrast in the tumor region (left base) is distinct compared to other regions (apex and anterior) for the patient case presented in Fig. 7, because of increased blood flow to prostate tumors than surroundings (48), future studies on a large number of patients with different types and grades of PCa would further help to elucidate the differential uptake of ICG in the malignant region. The maximum (75 mg) dose of ICG used in this study is well below the clinically permissible (2 mg/kg) and the highest dose previously injected (5 mg/kg) with no toxicity in humans (49–52). For further comparison, this dose is also quite lower than the average dose (10 mg/kg) of MRI contrast agents in humans (10, 53). Although increasing the ICG dose would further enhance the intraprostatic contrast and spectral ICG results, PA molecular imaging approaches that specifically target PCa biomarkers such as bombesin and prostate-specific membrane antigen (PSMA) (11, 18, 43), when integrated into the TRUSPA device, could improve the specificity of targeted biopsy and the ability to predict the prognosis and help induce focal therapy. There is a high potential for further improving the molecular sensitivity and depth of penetration

Fig. 7. Contrast-enhanced TRUSPA imaging of human prostate using intravenous ICG. A 53-year-old patient was diagnosed with PCa based on elevated PSA (5.33 ng/ml) and TRUS-guided biopsy showing Gleason 3 + 3 cancer in the left base of the prostate. Bladder (B), rectum (R), and prostate (P, green contour) are marked. (A) Diffusion-weighted MRI showing the malignancy (red contour) in the left PZ of the prostate. (B) Sagittal TRUS showing the MRI-based fused malignant (red) and control (yellow) regions used for the targeted biopsy. (C) Sagittal view of the 3D volume rendered patient's prostate based on MRI. Also shown is the schematic FOV of the TRUSPA device when imaging the peripheral lesion outlined in red in the left base with intravenous ICG (25 mg; 10 ml at 2.5 mg/ml). (D) Pre-ICG, (E) 2-min post-ICG, and (F) 6-min post-ICG images showing US (grayscale), PA (red), and co-registered US + PA images of the prostate. (G) Coefficient of first PCA, discussed in detail in fig. S11, plotted as a function of time relative to ICG injection. (H) Mean PA intensity in ROI 1 and ROI 2 as a function of wavelength plotted for pre- and post-ICG imaging periods. Spectrally unmixed ICG image (I) before and (J) after injecting ICG. (K) Pathology from prostatectomy showing a Gleason 3 + 4 cancer with extraprostatic extension and no cancer in lymph nodes, staged pt3aN0. Scale bars, 10 mm (A to F, I, and J). Yellow stickers on the red contour that surrounds the tumor region inside the tissue specimen show the dimensions 15.99 mm × 9.92 mm marked by the pathologist. (L) Magnification of a region inside the tumor outlined by red contour in (K). Scale bars, 1 mm (K) and 100 μ m (L).



(beyond 5 cm) of TRUSPA using a suitable combination of the following approaches: clinically translatable small molecules or nanoparticles with higher PA contrast than ICG (54), a model-based fluence correction for better spectral accuracy (55, 56), using more sensitive and larger CMUT (or other ultrasonic) arrays, advanced beamforming techniques such as spatial compounding (57), increasing light throughput from the current fluence of ~ 10 mJ/cm² to the ANSI safety allowing fluence of 30 mJ/cm² at 800 nm or 100 mJ/cm² at 1064 nm (41), and delivering light through the urethra (58). The effect of motion artifacts on the PA and US image quantitation using our TRUSPA probe will be also characterized in future studies.

Our present pilot clinical study has some limitations. First, we imaged a small number of patients ($n = 20$; 10 without and 10 with

intravenous ICG). More than 50% of cases had unknown cancer status, as their first TRUS-guided biopsy was performed after the TRUSPA imaging. Future clinical studies will image a large cohort of patient subjects with clinically relevant and insignificant PCa to further understand the diagnostic usefulness of TRUSPA measurements using robust statistical analysis. Second, the pathology results and the corresponding TRUSPA images of a patient might not be completely matched. However, given that the major pathological findings did not change from specimen to specimen within the tumor

Table 1. Statistical analysis on seven patients who received

intravenous ICG during the TRUSPA imaging. Slopes for change in the mean signal of the entire prostatic region between pre- and post-ICG injection for the measurements 800 nm (peak absorption of ICG), 950 nm (very low absorption of ICG), and unmixed ICG. Total of $n = 70$ measurements adjusted for dose and clustering within patient were used in the analysis. The fourth column “is slope = 0?” provides the probability for no change in signal difference between respective pre- and post-measures, and the fifth column “is slope = ICG slope?” provides the probability that the slope of a certain measurement (800 or 950 nm) follows the ICG slope.

Slope measure	Slope estimate	95% confidence interval for the estimated slope	Slope = 0? P	Slope = ICG slope? P
800 nm	3.5	-1.7 to 8.8	0.152	0.578
950 nm	0.9	-3.5 to 5.2	0.639	0.110
Unmixed ICG	4.9	1.8 to 8.1	0.009	

core region, our data suggest that the TRUSPA results can still be correlated to pathology results. Third, the maximum intravenous ICG dose is intentionally kept very well below the FDA-approved limits in these pilot studies, which limited the TRUSPA capabilities to further enhance intraprostatic PA contrast from vasculature structures and tumor regions. Fourth, the number of elements in the TRUSPA transducer and data acquisition system is also suboptimal compared to the conventional clinical TRUS machines. A current limitation of the CMUT technology is that they emit lower pressure compared to conventional PZT transducers. This is a result of the low inertia of the plate (thin plate, low mass) and can be further improved by optimizing CMUT cell design, such as incorporating a bump in the cavity (28). Despite these limitations, this study shows the possibility of using multispectral PAI to distinguish between endogenous (vascular) and exogenous (ICG) optical contrasts in the prostate, including potentially from the tumor region.

The TRUSPA system demonstrated here simultaneously unites PA-based molecular optical contrast with anatomical US of the prostate. The CMUT technology is a considerable improvement upon PZT-based systems for endoscopic PAI and displays potential for real-time 3D imaging of human prostate. In sharp contrast to limited information obtained from clinical TRUS, TRUSPA is capable of displaying vascular, functional, and biomarker-targeted molecular images of the disease and offers potential for new diagnostic and prognostic insights into PCa screening and management. Such a multiparametric TRUSPA system, combining all possible contrasts of conventional US, as well as PAI, has high potential to differentiate clinically relevant and insignificant PCa cancers, replace/reduce random biopsies with targeted biopsies, and help select suitable treatment options. In addition, TRUSPA can be easily integrated into the standard TRUS workflow in a urology clinic and could provide an attractive cost-effective alternative imaging platform to relatively expensive MRI and PET.

MATERIALS AND METHODS

Study design

The objectives of this prospective study were to develop, validate, and then clinically translate the TRUSPA device that uses miniaturized

CMUTs for human prostate imaging, and primarily investigate the intraprostatic PA contrast without and with the use of intravenous ICG injection in humans. The first set of validation studies was designed to test the deep-tissue imaging capabilities of the device using different tissue-mimicking phantoms as well as surgically removed intact human prostates ($n = 20$) from patients who underwent radical prostatectomy as a routine standard of care. In the next step, using mouse models of PCa ($n = 5$), the intravenous ICG imaging capabilities of the device were tested. These mouse studies were also designed to help test our quantitative spectral plotting and spectral unmixing methods using pre- and post-ICG injection multispectral PA data. The pilot clinical studies involving patients with PCa ($n = 20$; in which $n = 10$ with intravenous ICG) were designed to test the ability of the device to simultaneously image anatomical and vascular (including vascular perfusion) contrasts of the prostate in the US and PA modes of the device, respectively. The results of our initial trial are presented here as a feasibility study. The other study designs, along with methods, are provided in the following sections. All experiments involving humans and animals were approved by the IRB and Administrative Panel on Laboratory Animal Care, respectively, of the Stanford University. Informed consent was obtained from all participating patients.

Mouse PCa models

About 5 million PC3 cells [American Type Culture Collection (ATCC)] transfected with a lentivirus expressing both a green fluorescent protein (eGFP) and bioluminescent reporter gene *Luciferase* (*Luc2*) were implanted subcutaneously in the lower back of nude male mice ($n = 5$). Tumors were allowed to grow to a size of 50 to 1000 mm³ over about 3 weeks. Tumor growth and activity were monitored using bioluminescence imaging acquired by an IVIS 200 after intraperitoneal administration of substrate D-luciferin at a dose of 150 mg/kg (Biosynth).

In vivo transrectal imaging of human prostate without and with intravenous ICG

Patients with PCa with elevated serum PSA were first imaged with the TRUSPA device immediately before routine TRUS-guided biopsy procedure. Among the 20 patients we imaged, 10 without ICG and 10 with intravenous ICG (IC-Green, Akorn), only 5 patients had biopsy-proven PCa before the TRUSPA imaging. Hence, more than 50% of the patients we imaged had their first prostate biopsy after our TRUSPA studies, and their cancer status was not known during the TRUSPA study. As in conventional TRUS, the TRUSPA device was inserted into each patient's rectum and the prostate was visualized first in the US mode before starting the laser illumination for subsequent PA image acquisition. The device was linearly moved and/or rotated to visualize different regions of the prostate and surrounding structures such as the bladder at the urologist's discretion. Frame grabber software (Camtasia) recorded the video of time-lapse TRUSPA frames (each frame consisting of a US, PA, and a co-registered US + PA image) displayed on the computer screen. Raw US and PA data were saved for ROIs identified by the urologist and reconstructed using the delay-and-sum beamforming (59). Among the 10 ICG patients, the ICG dose was gradually increased from 5 mg (1 patient), 25 mg (2 patients), 50 mg (2 patients), to 75 mg (5 patients). The TRUSPA device was directed toward an ROI in the prostate, based on patient's preoperative MRI results, and was held still throughout the pre- and post-ICG imaging. To study the time activity of ICG (arrival and washing out) inside the prostate,

we acquired TRUSPA frames of 800 nm (the peak absorption wavelength of the ICG molecule) at multiple time points during the pre- and post-ICG sessions. To further study the presence of ICG inside the prostate—using the spectral plots and the spectral unmixing of oxyhemoglobin, deoxyhemoglobin, and ICG—we acquired multi-wavelength PA images from 750 to 950 nm in steps of 25 nm during the pre- and post-ICG time periods. The complete procedure took about 10 min.

PA data thresholding, time gain compensation, and spectral unmixing

Thresholding

The TRUSPA system SNR was studied under multiple imaging conditions including with laser ON and laser OFF conditions to understand inherent system-level noise. Our calculations showed that PA signal from a typical target in the laser ON image is more than 10 dB than the noise in the laser OFF image. We then studied the amount of noise in all our imaging conditions (phantoms, ex vivo tissue specimens, mice, and human studies) and applied thresholding on all PA images to bring them to an acceptable SNR of greater than 3 dB.

Time gain compensation settings

Depth-dependent time gain compensation (TGC) settings were applied for both US and PAI to compensate for the decrease in respective signal strengths with an increase in tissue depth.

Spectral unmixing

A nonnegative constraint-based linear spectral unmixing approach (60) was applied on multiwavelength PAI data that is compensated for variations in the laser output fluence as a function of wavelength, in addition to the thresholding and TGC as discussed above.

Statistical analysis of ICG patients

Intraprostatic ICG activity was analyzed using pre- and post-ICG PA measurements in 7 of 10 patients. Three patients were excluded: one patient with 5-mg ICG dose with negligible pre- and post-ICG difference, and two patients with high movement during the imaging. The five mean PA measurements of prostate used for the statistical analysis were as follows: (i) 800 nm at which ICG absorption is maximum; (ii) 950 nm with minimal absorption of ICG; and un-mixed images of (iii) ICG, (iv) oxyhemoglobin (HbO₂), and (v) deoxyhemoglobin (Hb). The statistical analysis was performed on the difference (slope) between these respective pre- and post-injection measurements. Table 1 presents slopes (positive if increase, negative if decrease) of 800 nm, 950 nm, and unmixed ICG measurements. A total of $n = 70$ measurements adjusted for dose and clustering within patients ($n = 7$) were used in the analysis of Table 1. Two null hypotheses were tested. One null hypothesis, “is slope = 0?”, provides the P value for no change in signal difference between respective pre- and post-measures; the other null hypothesis, “is slope = ICG slope?”, provides the P value for the slope of a certain measurement (800 or 950 nm) following the ICG slope.

SUPPLEMENTARY MATERIALS

stm.sciencemag.org/cgi/content/full/11/507/eaav2169/DC1

Materials and Methods

Fig. S1. Description of the TRUSPA imaging system next to the patient bed in the urology clinic.

Fig. S2. Schematics and images that describe the TRUSPA device, operating principle, and its data acquisition.

Fig. S3. Images of the CMUT array and ASIC.

Fig. S4. Simulated output pressure of a CMUT cell and experimental impedance measurements of a single CMUT element.

Fig. S5. Design and characterization of PDMS lens on the CMUT array.

Fig. S6. Time sequence used for simultaneous US and PAI of the TRUSPA device.

Fig. S7. Characterizing the US field of the TRUSPA device using simulations and experiments.

Fig. S8. Output pressure of the TRUSPA device, recorded by hydrophone in immersion, as a function of different DC and AC bias voltage settings.

Fig. S9. Characterization of TRUSPA system SNR as a function of depth and wavelength.

Fig. S10. Multiwavelength PA images of the mouse prostate tumor imaged with intravenous ICG.

Fig. S11. Multi-ROI time activity of ICG for the patient case presented in Fig. 7.

Fig. S12. Multiwavelength PA images of human prostate for the patient case presented in Fig. 7.

Fig. S13. Analysis of ICG activity during in vivo TRUSPA imaging of a human patient with PCA intravenously administered 75 mg of ICG at a concentration of 2.5 mg/ml.

Fig. S14. Analysis of ICG activity during in vivo TRUSPA imaging of a human patient with PCA intravenously administered 5 mg of ICG at a concentration of 2.5 mg/ml.

Table S1. 1D (linear) CMUT array parameters.

Table S2. Typical deep-tissue imaging parameters of the TRUSPA device.

Table S3. Intravenous ICG dose given to 10 human subjects at a concentration of 2.5 mg/ml. Movie S1. In vivo TRUSPA imaging of human prostate in clinic (without administering contrast agent).

REFERENCES AND NOTES

1. J. Ferlay, I. Soerjomataram, R. Dikshit, S. Eser, C. Mathers, M. Rebelo, D. M. Parkin, D. Forman, F. Bray, Cancer incidence and mortality worldwide: Sources, methods and major patterns in GLOBOCAN 2012. *Int. J. Cancer* **136**, E359–E386 (2015).
2. F. H. Schröder, J. Hugosson, M. J. Roobol, T. L. J. Tammela, S. Ciatto, V. Nelen, M. Kwiatkowski, M. Lujan, H. Lilja, M. Zappa, L. J. Denis, F. Recker, A. Berenguer, L. Mänttinen, C. H. Bangma, G. Aus, A. Villers, X. Rebillard, T. van der Kwast, B. G. Blijenberg, S. M. Moss, H. J. de Koning, A. Auvinen; ERSPC Investigators, Screening and prostate-cancer mortality in a randomized European study. *N. Engl. J. Med.* **360**, 1320–1328 (2009).
3. C. E. Barbieri, S. C. Baca, M. S. Lawrence, F. Demichelis, M. Blattner, J.-P. Theurillat, T. A. White, P. Stojanov, E. Van Allen, N. Stransky, E. Nickerson, S.-S. Chae, G. Boysen, D. Auclair, R. C. Onofrio, K. Park, N. Kitabayashi, T. Y. MacDonald, K. Sheikh, T. Vuong, C. Guiducci, K. Cibulskis, A. Sivachenko, S. L. Carter, G. Saksena, D. Voet, W. M. Hussain, A. H. Ramos, W. Winckler, M. C. Redman, K. Ardlie, A. K. Tewari, J. M. Mosquera, N. Rupp, P. J. Wild, H. Moch, C. Morrissey, P. S. Nelson, P. W. Kantoff, S. B. Gabriel, T. R. Golub, M. Meyerson, E. S. Lander, G. Getz, M. A. Rubin, L. A. Garraway, Exome sequencing identifies recurrent *SPOP*, *FOXA1* and *MED12* mutations in prostate cancer. *Nat. Genet.* **44**, 685–689 (2012).
4. G. M. Cann, Z. G. Gulzar, S. Cooper, R. Li, S. Luo, M. Tat, S. Stuart, G. Schroth, S. Srinivas, M. Ronaghi, J. D. Brooks, A. H. Talasz, mRNA-Seq of single prostate cancer circulating tumor cells reveals recapitulation of gene expression and pathways found in prostate cancer. *PLOS ONE* **7**, e49144 (2012).
5. S. A. Tomlins, J. R. Day, R. J. Lonigro, D. H. Hovelson, J. Siddiqui, L. P. Kunju, R. L. Dunn, S. Meyer, P. Hodge, J. Groskopf, J. T. Wei, A. M. Chinnaiyan, Urine *TMPRSS2:ERG* plus PCA3 for individualized prostate cancer risk assessment. *Eur. Urol.* **70**, 45–53 (2016).
6. M. L. Palmeri, T. J. Glass, Z. A. Miller, S. J. Rosenzweig, A. Buck, T. J. Polascik, R. T. Gupta, A. F. Brown, J. Madden, K. R. Nightingale, Identifying clinically significant prostate cancers using 3-D in vivo acoustic radiation force impulse imaging with whole-mount histology validation. *Ultrasound Med. Biol.* **42**, 1251–1262 (2016).
7. S. Li, J. Kim, Z. Wang, X. Jiang, S. Kasoji, B. Lindsey, P. A. Dayton, A 3 MHz/18 MHz dual-layer co-linear array for transrectal acoustic angiography, in *IEEE International Ultrasonics Symposium* (IEEE, 2015).
8. Y. Chen, M. Nguyen, J. T. Yen, A 5-MHz cylindrical dual-layer transducer array for 3-D transrectal ultrasound imaging. *Ultrasound Imaging* **34**, 181–195 (2012).
9. M. Gayet, A. van der Aa, H. P. Beerlage, B. P. Schrier, P. F. A. Mulders, H. Wijkstra, The value of magnetic resonance imaging and ultrasonography (MRI/US)-fusion biopsy platforms in prostate cancer detection: A systematic review. *BJU Int.* **117**, 392–400 (2016).
10. S. J. Nelson, J. Kurhanewicz, D. B. Vigneron, P. E. Z. Larson, A. L. Harzstark, M. Ferrone, M. van Criekinge, J. W. Chang, R. Bok, I. Park, G. Reed, Metabolic imaging of patients with prostate cancer using hyperpolarized [¹³C] pyruvate. *Sci. Transl. Med.* **5**, 198ra108 (2013).
11. A. Afshar-Oromieh, C. M. Zechmann, A. Malcher, M. Eder, M. Eisenhut, H. G. Linhart, T. Holland-Letz, B. A. Hadaschik, F. L. Giesel, J. Debus, U. Haberkorn, Comparison of PET imaging with a ⁶⁸Ga-labelled PSMA ligand and ¹⁸F-choline-based PET/CT for the diagnosis of recurrent prostate cancer. *Eur. J. Nucl. Med. Mol. Imaging* **41**, 11–20 (2014).
12. Y. Zhou, D. Wang, Y. Zhang, U. Chitgupi, J. Geng, Y. Wang, Y. Zhang, T. R. Cook, J. Xia, J. F. Lovell, A phosphorus phthalocyanine formulation with intense absorbance at 1000 nm for deep optical imaging. *Theranostics* **6**, 688–697 (2016).
13. L. V. Wang, S. Hu, Photoacoustic tomography: In vivo imaging from organelles to organs. *Science* **335**, 1458–1462 (2012).

14. V. Ntziachristos, J. Ripoll, L. V. Wang, R. Weissleder, Looking and listening to light: The evolution of whole-body photonic imaging. *Nat. Biotechnol.* **23**, 313–320 (2005).
15. E. Z. Zhang, J. G. Laufer, R. B. Pedley, P. C. Beard, In vivo high-resolution 3D photoacoustic imaging of superficial vascular anatomy. *Phys. Med. Biol.* **54**, 1035–1046 (2009).
16. D. R. Bauer, R. Olafsson, L. G. Montilla, R. S. Witte, 3-D photoacoustic and pulse echo imaging of prostate tumor progression in the mouse window chamber. *J. Biomed. Opt.* **16**, 026012 (2011).
17. A. De La Zerda, C. Zavaleta, S. Keren, S. Vaithilingam, S. Bodapati, Z. Liu, J. Levi, B. R. Smith, T.-J. Ma, O. Oralkan, Z. Cheng, X. Chen, H. Dai, B. T. Khuri-Yakub, S. S. Gambhir, Carbon nanotubes as photoacoustic molecular imaging agents in living mice. *Nat. Nanotechnol.* **3**, 557–562 (2008).
18. J. Levi, A. Sathirachinda, S. S. Gambhir, A high-affinity, high-stability photoacoustic agent for imaging gastrin-releasing peptide receptor in prostate cancer. *Clin. Cancer Res.* **20**, 3721–3729 (2014).
19. M. Heijblom, D. Piras, W. Xia, J. C. G. Van Hespren, J. M. Klaase, F. M. van den Engh, T. G. van Leeuwen, W. Steenbergen, S. Manohar, Visualizing breast cancer using the Twente photoacoustic mammoscope: What do we learn from twelve new patient measurements? *Opt. Express* **20**, 11582–11597 (2012).
20. A. Garcia-Urbe, T. N. Erpelding, A. Krumholz, H. Ke, K. Maslov, C. Appleton, J. A. Margenthaler, L. V. Wang, Dual-modality photoacoustic and ultrasound imaging system for noninvasive sentinel lymph node detection in patients with breast cancer. *Sci. Rep.* **5**, 15748 (2015).
21. S. A. Ermilov, T. Khamapirad, A. Conjusteau, M. H. Leonard, R. Laceywell, K. Mehta, T. Miller, A. A. Oraevsky, Laser optoacoustic imaging system for detection of breast cancer. *J. Biomed. Opt.* **14**, 024007 (2009).
22. P. D. Kumavor, U. Alqasemi, B. Tavakoli, H. Li, Y. Yang, X. Sun, E. Warych, Q. Zhu, Co-registered pulse-echo/photoacoustic transvaginal probe for real time imaging of ovarian tissue. *J. Biophotonics* **6**, 475–484 (2013).
23. X. Wang, W. W. Roberts, P. L. Carson, D. P. Wood, J. B. Fowlkes, Photoacoustic tomography: A potential new tool for prostate cancer. *Biomed. Opt. Express* **1**, 1117–1126 (2010).
24. M. A. Yaseen, S. A. Ermilov, H.-P. F. Brecht, R. Su, A. Conjusteau, M. P. Fronheiser, B. A. Bell, M. Motamedi, A. A. Oraevsky, Optoacoustic imaging of the prostate: Development toward image-guided biopsy. *J. Biomed. Opt.* **15**, 021310 (2010).
25. M. A. Lediju Bell, N. P. Kuo, D. Y. Song, J. U. Kang, E. M. Boctor, In vivo visualization of prostate brachytherapy seeds with photoacoustic imaging. *J. Biomed. Opt.* **19**, 126011 (2014).
26. A. Horiguchi, K. Tsujita, K. Irisawa, T. Kasamatsu, K. Hirota, M. Kawaguchi, M. Shinchi, K. Ito, T. Asano, H. Shinmoto, H. Tsuda, A pilot study of photoacoustic imaging system for improved real-time visualization of neurovascular bundle during radical prostatectomy. *Prostate* **76**, 307–315 (2016).
27. A. Horiguchi, M. Shinchi, A. Nakamura, T. Wada, K. Ito, T. Asano, H. Shinmoto, H. Tsuda, M. Ishihara, Pilot study of prostate cancer angiogenesis imaging using a photoacoustic imaging system. *Urology* **108**, 212–219 (2017).
28. M. Ishihara, A. Horiguchi, H. Shinmoto, H. Tsuda, K. Irisawa, T. Wada, T. Asano, Comparison of transrectal photoacoustic, Doppler, and magnetic resonance imaging for prostate cancer detection. *Proc. SPIE* **9708**, 970852 (2016).
29. A. Nikoozadeh, B. Bayram, G. G. Yaralioglu, B. T. Khuri-Yakub, Analytical calculation of collapse voltage of CMUT membrane. *IEEE Int. Ultrason. Symp.* **1**, 256–259 (2004).
30. K. K. Park, H. Lee, M. Kupnik, B. T. Khuri-Yakub, Fabrication of capacitive micromachined ultrasonic transducers via local oxidation and direct wafer bonding. *J. Microelectromech. Syst.* **20**, 95–103 (2011).
31. M. Engholm, H. Bouzari, T. L. Christiansen, C. Beers, J. P. Bagge, L. N. Moesner, S. E. Diederichsen, M. B. Stuart, J. A. Jensen, E. V. Thomsen, Probe development of CMUT and PZT row-column-addressed 2-D arrays. *Sens. Actuat. A Phys.* **273**, 121–133 (2018).
32. M. Vallet, F. Varray, J. Boutet, J.-M. Dinten, G. Caliano, A. S. Savoia, D. Vray, Quantitative comparison of PZT and CMUT probes for photoacoustic imaging: Experimental validation. *Photoacoustics* **8**, 48–58 (2017).
33. O. Warshavski, C. Meynier, N. S en egond, P. Chatain, J. Rebling, D. Razansky, N. Felix, A. Nguyen-Dinh, Experimental evaluation of cMUT and PZT transducers in receive only mode for photoacoustic imaging, in *Proc. SPIE 9708, Photons Plus Ultrasound: Imaging and Sensing* (SPIE, 2016).
34. P. Cristman, O. Oralkan, X. Zhuang, T.-J. Ma, S. Vaithilingam, T. Carver, I. Wygant, B. T. Khuri-Yakub, A 2D CMUT hydrophone array: Characterization results, in *IEEE International Ultrasonics Symposium* (IEEE, 2009).
35. I. O. Wygant, X. Zhuang, D. Yeh, O. Oralkan, A. S. Ergun, M. Karaman, B. T. Khuri-Yakub, Integration of 2D CMUT arrays with front-end electronics for volumetric ultrasound imaging. *IEEE Trans. Ultrason. Ferroelectr. Freq. Control* **55**, 327–342 (2008).
36. O. Oralkan, B. Bayram, G. G. Yaralioglu, A. S. Ergun, M. Kupnik, D. T. Yeh, I. O. Wygant, B. T. Khuri-Yakub, Experimental characterization of collapse-mode CMUT operation. *IEEE Trans. Ultrason. Ferroelectr. Freq. Control* **53**, 1513–1523 (2006).
37. S.-R. Kothapalli, T.-J. Ma, S. Vaithilingam, O. Oralkan, B. T. Khuri-Yakub, S. S. Gambhir, Deep tissue photoacoustic imaging using a miniaturized 2-D capacitive micromachined ultrasonic transducer array. *IEEE Trans. Biomed. Eng.* **59**, 1199–1204 (2012).
38. X. Zhuang, A. Nikoozadeh, M. A. Beasley, G. G. Yaralioglu, B. T. Khuri-Yakub, B. L. Pruitt, Biocompatible coatings for CMUTs in a harsh, aqueous environment. *J. Micromech. Microeng.* **17**, 994–1001 (2007).
39. L. V. Wang, R. E. Nordquist, W. R. Chen, Optimal beam size for light delivery to absorption enhanced tumors buried in biological tissues and effect of multiple-beam delivery: A Monte Carlo study. *Appl. Optics* **36**, 8286–8291 (1997).
40. J. A. Jensen, Field: A program for simulating ultrasound systems. *Med. Biol. Eng. Comput.* **34**, 351–353 (1996).
41. Laser Institute of America, *American National Standard for Safe Use of Lasers* (American National Standards Institute, Inc., 2000).
42. T. Svensson, S. Andersson-Engels, M. Einarsdottir, K. Svanberg, In vivo optical characterization of human prostate tissue using near-infrared time-resolved spectroscopy. *J. Biomed. Opt.* **12**, 014022 (2007).
43. R. Minamimoto, S. Hancock, B. Schneider, F. T. Chin, M. Jamali, A. Loening, S. Vasanawala, S. S. Gambhir, A. Igaru, Pilot comparison of ⁶⁸Ga-RM2 PET and ⁶⁸Ga-PSMA-11 PET in patients with biochemically recurrent prostate cancer. *J. Nucl. Med.* **57**, 557–562 (2016).
44. C. Zhang, K. Maslov, L. V. Wang, Subwavelength-resolution label-free photoacoustic microscopy of optical absorption in vivo. *Opt. Lett.* **35**, 3195–3197 (2010).
45. National Center for Biotechnology Information, PubChem Compound Database; <https://pubchem.ncbi.nlm.nih.gov/compound/11967809> [accessed 19 February 2017].
46. K. J. Baker, Binding of sulfobromophthalein (BSP) sodium and indocyanine green (ICG) by plasma α -1 lipoproteins. *Exp. Biol. Med.* **122**, 957–963 (1966).
47. G. R. Cherrick, S. W. Stein, C. M. Leevy, C. S. Davidson, Indocyanine green: Observations on its physical properties, plasma decay, and hepatic extraction. *J. Clin. Invest.* **39**, 592–600 (1960).
48. D. L. Buckley, C. Roberts, G. J. M. Parker, J. P. Logue, C. E. Hutchinson, Prostate cancer: Evaluation of vascular characteristics with dynamic contrast-enhanced T1-weighted MR imaging—Initial experience. *Radiology* **233**, 709–715 (2004).
49. J. T. Alander, I. Kaartinen, A. Laakso, T. P atil a, T. Spillmann, V. V. Tuchin, M. Venermo, P. V alisuo, A review of indocyanine green fluorescent imaging in surgery. *Int. J. Biomed. Imaging* **2012**, 940585 (2012).
50. G. Paumgartner, The handling of indocyanine green by the liver. *Schweiz. Med. Wochenschr.* **105**, 1–30 (1975).
51. P. Probst, G. Paumgartner, H. Caucig, H. Fr ohlich, G. Grabner, Studies on clearance and placental transfer of indocyanine green during labor. *Clin. Chim. Acta* **29**, 157–160 (1970).
52. Akorn Inc., *IC-GREEN (Indocyanine Green for Injection, USP) Product Monograph* (Akorn Inc., 2006).
53. M. R. Prince, C. Arnoldus, J. K. Frisoli, Nephrotoxicity of high-dose gadolinium compared with iodinated contrast. *J. Magn. Reson. Imaging* **6**, 162–166 (1996).
54. Y.-S. Chen, W. Frey, S. Kim, P. Kruizinga, K. Homan, S. Emelianov, Silica-coated gold nanorods as photoacoustic signal nanoamplifiers. *Nano Lett.* **11**, 348–354 (2011).
55. X. L. Dean-Ben, A. Buehler, V. Ntziachristos, D. Razansky, Accurate model-based reconstruction algorithm for three-dimensional optoacoustic tomography. *IEEE Trans. Med. Imaging* **31**, 1922–1928 (2012).
56. B. T. Cox, S. R. Arridge, P. C. Beard, Estimating chromophore distributions from multiwavelength photoacoustic images. *J. Opt. Soc. Am. A* **26**, 443–455 (2009).
57. H. J. Kang, M. A. L. Bell, X. Guo, E. M. Boctor, Spatial angular compounding of photoacoustic images. *IEEE Trans. Med. Imaging* **35**, 1845–1855 (2016).
58. M. A. L. Bell, X. Guo, D. Y. Song, E. M. Boctor, Transurethral light delivery for prostate photoacoustic imaging. *J. Biomed. Opt.* **20**, 036002 (2015).
59. S. R. Kothapalli, Simultaneous transrectal ultrasound and photoacoustic human prostate imaging (version 1.0) (Zenodo, 2019); <http://doi.org/10.5281/zenodo.3347969>.
60. C. L. Lawson, R. J. Hanson, *Solving Least-Squares Problems* (Prentice Hall, 1974), chap. 23, p. 161.

Acknowledgments: We thank J. Rosenberg for the statistical analysis of ICG patient data. We thank laboratory members of S.S.G. and P.T.K.-Y. for their help and discussions. We thank the Stanford Nanofabrication Facility for their support in the fabrication of capacitive micromachined ultrasonic arrays. Part of the TRUSPA integration design and fabrication work was done in the Stanford Nano Shared Facilities (supported by the NSF, ECCS-1542152). We also extend our thanks to the National Semiconductors for their support in the fabrication of ASICs. We thank K. Merkle and his team in the physics machine shop at Stanford for the fabrication of polycarbonate housing of the TRUSPA device. We thank summer undergraduate interns A. Lei and R. Singh for their assistance in some phantom and mice experiments with TRUSPA. We thank laboratory members of J.C.L. for their assistance in experiments with surgically removed prostates. We thank K. Rupnarayan for help with consenting the PCA patients. We thank A. Karanay for assistance with intravenous ICG experiments and J. Schwimmer for help with proofreading the manuscript. **Funding:** We acknowledge funding

support from NCI ICMIC P50CA114747 (S.S.G.), NCI CCNE-T U54 U54CA151459 (S.S.G.), the Canary Foundation (S.S.G.), RO1HL117740 (P.T.K.-Y.), NIBIB-K99EB017729 (S.-R.K.), NIBIB-R00EB017729-04 (S.-R.K.), the Sir Peter Michael Foundation (S.S.G. and S.-R.K.), Philips Medical (S.S.G.), and T32-CA118681 (D.M.H.). This work was supported in part from a grant by Philips Healthcare (S.S.G.). **Author contributions:** S.S.G. conceived the idea of PAI of the human prostate and supervised the entire bench-to-bedside clinical translation of the project. S.-R.K. designed the integrated TRUSPA device, including the fiber optic cable, the polycarbonate housing, and the PCB cable for CMUT and ASIC bonding; A.N. and P.T.K.-Y. contributed to the PCB design. J.W.C. and M.F.R. developed the real-time imaging software on Verasonics platform. S.-R.K. developed the beamforming code for the raw RF data reconstruction used in all the data analysis, the spectral unmixing code, the spectral analysis approach, and the control sequence for synchronizing the laser firing with the data acquisition system. K.K.P. and P.T.K.-Y. designed and fabricated the CMUT array. A.B. and P.T.K.-Y. developed ASICs. S.-R.K., T.E.C., and P.T.K.-Y. designed the PDMS lens mold. S.-R.K. and T.E.C. integrated all components of the TRUSPA device with PDMS encapsulation. S.-R.K., A.B., B.C.L., P.C., A.N., and A.M. performed the characterization of the CMUT arrays, ASICs, and the TRUSPA US field distribution using the hydrophone. S.-R.K. performed Field II simulations and all validation experiments in phantoms, mice models of cancer, and surgically removed human prostates. S.-R.K. set up all the in vivo TRUSPA experiments in the urology clinic and assisted in the data acquisition, whereas G.A.S. and L.S. performed transrectal imaging in men using the TRUSPA device and prepared the ICG solutions for intravenous injection. S.-R.K., S.S.G., G.A.S., J.W., J.D.B., J.C.L., and R.F. contributed to the protocols for the patient imaging. D.T. and J.C.L. provided surgically removed human

prostates and contributed to the interpretation and analysis. S.-R.K., G.A.S., J.D.B., J.C.L., and S.S.G. interpreted TRUSPA imaging results. I.S. and D.M.H. assisted in the last five ICG experiments. S.-R.K. wrote the main and supplementary manuscripts, and all authors provided comments and suggestions to further improve the clarity of the manuscript. **Competing interests:** S.S.G. serves on the board of Endra Inc. (a manufacturer of small-animal PA instruments and RF-acoustic instruments), is a founding member, and has stock options. S.S.G. also served as a paid consultant to VisualSonics (a developer of US and PA products) up to late 2017. **Data and materials availability:** All data associated with this study are present in the paper and/or the Supplementary Materials. The software associated with US and PA beamforming using the raw RF data, and spectral unmixing using the multispectral PA data is available at <http://doi.org/10.5281/zenodo.3347969>.

Submitted 25 August 2018

Accepted 26 July 2019

Published 28 August 2019

10.1126/scitranslmed.aav2169

Citation: S.-R. Kothapalli, G. A. Sonn, J. W. Choe, A. Nikoozadeh, A. Bhuyan, K. K. Park, P. Cristman, R. Fan, A. Moini, B. C. Lee, J. Wu, T. E. Carver, D. Trivedi, L. Shiiba, I. Steinberg, D. M. Huland, M. F. Rasmussen, J. C. Liao, J. D. Brooks, P. T. Khuri-Yakub, S. S. Gambhir, Simultaneous transrectal ultrasound and photoacoustic human prostate imaging. *Sci. Transl. Med.* **11**, eaav2169 (2019).

Science Translational Medicine

Simultaneous transrectal ultrasound and photoacoustic human prostate imaging

Sri-Rajasekhar Kothapalli, Geoffrey A. Sonn, Jung Woo Choe, Amin Nikoozadeh, Anshuman Bhuyan, Kwan Kyu Park, Paul Cristman, Richard Fan, Azadeh Moini, Byung Chul Lee, Jonathan Wu, Thomas E. Carver, Dharati Trivedi, Lillian Shiiba, Idan Steinberg, David M. Huland, Morten F. Rasmussen, Joseph C. Liao, James D. Brooks, Pierre T. Khuri-Yakub and Sanjiv S. Gambhir

Sci Transl Med 11, eaav2169.
DOI: 10.1126/scitranslmed.aav2169

Probing the prostate

Molecular imaging can help improve detection of cancer, but some modalities require ionizing radiation, making them nonideal for repeated imaging. Kothapalli *et al.* developed a probe that could perform ultrasound and photoacoustic imaging simultaneously, two modalities that do not require ionizing radiation. Testing the transrectal ultrasound and photoacoustic device in vitro, in mouse models, and using excised human prostates demonstrated the ability to view anatomical features within tissue and vascular contrast within tumors. Administering a dye improved photoacoustic contrast when imaging the prostates of human subjects with cancer. This device allows for real-time anatomical, functional, and molecular imaging of the human prostate and could be easily adopted into clinical workflows.

ARTICLE TOOLS

<http://stm.sciencemag.org/content/11/507/eaav2169>

SUPPLEMENTARY MATERIALS

<http://stm.sciencemag.org/content/suppl/2019/08/26/11.507.eaav2169.DC1>

RELATED CONTENT

<http://stm.sciencemag.org/content/scitransmed/5/198/198ra108.full>
<http://stm.sciencemag.org/content/scitransmed/11/503/eaaw4993.full>
<http://stm.sciencemag.org/content/scitransmed/7/271/271ra7.full>
<http://stm.sciencemag.org/content/scitransmed/11/498/eaaw4636.full>

REFERENCES

This article cites 52 articles, 4 of which you can access for free
<http://stm.sciencemag.org/content/11/507/eaav2169#BIBL>

PERMISSIONS

<http://www.sciencemag.org/help/reprints-and-permissions>

Use of this article is subject to the [Terms of Service](#)

Science Translational Medicine (ISSN 1946-6242) is published by the American Association for the Advancement of Science, 1200 New York Avenue NW, Washington, DC 20005. 2017 © The Authors, some rights reserved; exclusive licensee American Association for the Advancement of Science. No claim to original U.S. Government Works. The title *Science Translational Medicine* is a registered trademark of AAAS.